Wavelet-based Optical Flow for High-Resolution Velocimetry in Wall-Bounded Fluid Flows

Alexander Nicolas[1,*], Florian Zentgraf[2], Mark Linne[1], Andreas Dreizler[2], Brian Peterson[1]

1: Institute for Multiscale Thermofluids, The University of Edinburgh, United Kingdom
2: Reactive Flow and Diagnostics, Technical University of Darmstadt, Germany
*Corresponding author: alexander.nicolas@ed.ac.uk

Keywords: PIV, boundary layer, turbulence, optical flow, velocimetry

ABSTRACT

The performance of a wavelet-based optical flow velocimetry (wOFV) algorithm in extracting high accuracy and high resolution velocity fields from tracer particle images in wall-bounded flows is assessed. wOFV is first evaluated using a DNS database of a turbulent boundary layer, which served as ground truth synthetic data. The sensitivity of wOFV to the regularization parameter (λ) is quantified and results are compared to commercially available PIV cross-correlation-based processing. Results on synthetic data indicate a slight preference towards under-regularization in the viscous sublayer region to minimise error. Nonetheless, tests on synthetic data reveal that wOFV can modestly outperform PIV in terms of accuracy for a broad λ range. For the synthetic dataset, wOFV revealed clear advantages over PIV in terms of vector resolution, being able to resolve 29 vectors in the viscous sublayer (versus 5 for PIV) and provide 13 vectors closer to the wall than PIV. wOFV was also applied to experimental data of a turbulent boundary layer near the leading edge of a side-wall quenching burner setup and compared to PIV. Good agreement between the two velocimetry techniques was found, with wOFV exhibiting superior vector resolution. Based on theoretical relations of the viscous sublayer, a physically justified λ weighting for wOFV was determined. With this setting, wOFV was able to resolve further and more accurately into the viscous sublayer. Analysis of the turbulent velocity fluctuations revealed some spurious results for PIV in close proximity to the wall, leading to significantly exaggerated turbulence intensity in the viscous sublayer region. wOFV did not exhibit this same effect, revealing that it is less biased by the presence of the wall and decreased image signal-to-noise ratio. These aspects show that wOFV can provide improved accuracy and reliability in resolving turbulent motion occurring in the vicinity of physical boundaries.

1. Introduction

Fluid flow dynamics and the interaction with walls are of prime importance in a variety of engineering applications. The dynamics of the boundary layer region are of major interest and have been the subject of extensive research since the fundamental work of (Prandtl, 1904). Many industrially, biologically, and medically relevant flows require detailed knowledge and understanding of the flow near boundaries which must be achieved or validated through experimental measurements.

The mean shear stress exerted on a wall is a particularly important parameter in boundary layer research:

$$\tau_w = \mu \frac{\partial \langle U_1 \rangle}{\partial x_2} \big|_{x_2=0} = \mu \gamma \tag{1}$$

where μ is the dynamic viscosity, $\langle U_1 \rangle$ is the mean streamwise velocity and x_2 is the wall normal distance coordinate. In turbulence studies, boundary layer quantities are typically normalised using an inner scaling based on the friction velocity defined by:

$$u_\tau = \sqrt{\frac{\tau_w}{\rho}} \tag{2}$$

where ρ is the fluid density. The normalisation of boundary layer quantities using the friction velocity u_τ is essential in facilitating comparison between theoretical, numerical and experimental results. In particular, the mean streamwise velocity profile and the wall-normal distance coordinate are normalised to 'wall units' by the friction velocity:

$$u^+ = \frac{\langle U_1 \rangle}{u_\tau} \tag{3}$$

$$y^+ = x_2 \frac{u_\tau}{\nu} \tag{4}$$

where ν is kinematic viscosity. For flows with constant physical properties, it can be seen from equation (2) that the normalising variable u_τ is ultimately defined by the wall shear stress τ_w and therefore the estimate of the velocity gradient at the wall γ from equation (1). The accurate estimation of the velocity gradient γ at the wall is therefore crucial for accurate scaling and subsequent evaluation of boundary layer quantities.

Non-intrusive flow measurement techniques such as digital correlation-based particle image velocimetry (PIV) and particle tracking velocimetry (PTV) have become well established for boundary layer investigations (Raffel et al., 2018) (Willert, 2015) (Schröder et al., 2011) (Renaud et al., 2018) (Ding et al., 2019). PIV, however, is well known to have fundamental limitations in spatial resolution (Kähler et al., 2012a) which can present challenges for obtaining reliable velocity measurements in the vicinity of the wall. PTV can significantly improve on this aspect (Kähler et al., 2012b), but is more sensitive to image signal-to-noise ratio (SNR) and particle seeding density (Kähler et al., 2016).

A promising alternative to these traditional velocimetry techniques is a method from computer vision literature known as optical flow (Horn & Schunck, 1981). Application of optical flow velocimetry (OFV) techniques have previously demonstrated increased accuracy and resolution over conventional correlation-based methods (e.g. (Yuan et al., 2007) (Corpetti et al., 2006) (Ruhnau et al., 2007) (Héas et al., 2012) (Dérian et al., 2013) (Kadri-Harouna et al., 2013) (Schmidt & Sutton, 2019)). These studies have primarily focused on synthetic and experimental test cases involving analytical flows, isotropic turbulence and free shear flows. Despite its capabilities, few applications of OFV applied to wall-bounded flows exist in the literature (Kapulla et al., 2011) (Kähler et al., 2016) (Stanislas et al., 2005) (Ruhnau & Schnörr, 2006) (Stark, 2013). Such studies primarily demonstrate the use of OFV in wall-bounded environments and limit investigation to velocity profiles. A detailed analysis of derived quantities such as the wall-shear stress as well as

evaluation of accuracy and resolution of the inner-scaled turbulent boundary layer quantities is absent in the literature.

The present work assesses the performance of an advanced wavelet-based optical flow velocimetry (wOFV) method in the context of turbulent wall-bounded flows. The influence of a regularization parameter, common in OFV techniques, is investigated on resolving both instantaneous flow properties and statistics to gain detailed insight and understanding on its effect. A sensitivity study in comparison to results from correlation-based PIV processing is performed using synthetic particle images generated from DNS of a turbulent channel flow. wOFV is then applied to an experimental PIV dataset of a side-wall burner quenching (SWQ) setup run under turbulent non-reacting conditions. Results are compared to correlation-based PIV processing to demonstrate the advantages of wOFV as an alternative technique in the study of turbulent wall-bounded flows.

2. Optical flow

Optical flow is the apparent displacement of brightness intensity patterns in an image sequence (Horn & Schunck, 1981). The basic assumption in most optical flow techniques is the conservation of pixel brightness intensity between images. This can be expressed as the displaced frame difference (DFD):

$$I_0(\mathbf{x}) - I_1(\mathbf{x} + \mathbf{U}(\mathbf{x})) = 0 \tag{5}$$

where $I(\mathbf{x})$ is the brightness intensity at pixel locations $\mathbf{x} = (x_1, x_2)^T$ in the image domain Ω and $\mathbf{U}(\mathbf{x}) = (U_1(\mathbf{x}), U_2(\mathbf{x}))^T$ is the two-dimensional displacement. The displacement field $\mathbf{U}(\mathbf{x})$ in the DFD is determined using a minimisation problem of the form:

$$\hat{\mathbf{U}} = \arg\min_{\mathbf{U}} J_D(I_0, I_1, \mathbf{U}) + \lambda J_R(\mathbf{U}) \tag{6}$$

J_D is known as the data term which includes equation 5 into a penalty function, commonly a quadratic penalty, as in the current work. The regularization term fills in information about the velocity field to compensate for regions where motion cannot be determined from the data term alone. J_R affects the spatial coherence of neighbouring velocity vectors and enforces a degree of regularity or visually perceived "smoothness" to the velocity field. The present work uses the high-order Laplacian regularization in a quadratic penalty:

$$J_R = \int_{\Omega} |\nabla^2 U_1|^2 + |\nabla^2 U_2|^2 d\Omega \tag{7}$$

The parameter λ establishes the relative importance of J_D versus J_R during the minimisation process. Lower λ values result in better matching of pixel intensities between I_0 to I_1 to reduce the DFD even if the estimated flow field is non-physical and noisy. Increasing λ dampens small-scale motion and noise, eventually leading to an excessive smoothing of the velocity field at higher values. Correct selection of the regularization parameter λ is important to obtain accurate velocity fields in OFV. Other works exploring and discussing this parameter in the context of fluid velocimetry are limited to those of (Corpetti et al., 2002), (Kapulla et al., 2011) , Stark (2013), (Schmidt

& Sutton, 2019), (Cai et al., 2018), (Heás et al., 2013). None of these, however, have investigated the sensitivity of λ specifically in relation to near-wall measurements in wall-bounded flows, where the motion discontinuity caused by the wall may be particularly affected by the smoothing process (Black & Anandan, 1996) (Aubert et al., 1999).

In contrast to other OFV techniques, the wavelet-based method performs the minimisation of equation 6, not over the physical velocity field $\mathbf{U}(\mathbf{x})$, but over the wavelet coefficients $\boldsymbol{\Theta} = (\Theta_1, \Theta_2)^T$ from its discrete wavelet transform (DWT) $\boldsymbol{\Theta} = \Psi^{-1}(\mathbf{x})\mathbf{U}(\mathbf{x})$ where $\Psi^{-1}(\mathbf{x})$ denotes the wavelet transform decomposition operator. A wavelet transform extracts the frequency content of a signal (or image in 2D) at different scales of resolution (Mallat, 2009). Broadly speaking, wOFV can be considered a type of parameterisation of classical OFV approaches in terms of wavelet coefficients to be solved for:

$$\hat{\boldsymbol{\Theta}} = \arg\min_{\boldsymbol{\Theta}} J_D(I_0, I_1, \boldsymbol{\Theta}) + \lambda J_R(\boldsymbol{\Theta}) \tag{8}$$

Once the full minimisation is complete, the velocity field in physical space is recovered by application of the DWT reconstruction operator $\Psi(\mathbf{x})$ to the output wavelet coefficients $\Psi(\mathbf{x})\hat{\boldsymbol{\Theta}} = \hat{\mathbf{U}}$. The wavelet framework provides a natural and effective multiresolution framework in which to perform the minimisation of equation 8. Details of the wOFV algorithm can be found in (Dérian et al., 2013) (Kadri-Harouna et al., 2013) (Schmidt & Sutton, 2019) (Schmidt & Sutton, 2020).

3. Description of synthetic test case

In order to quantitatively assess wOFV performance and λ parameter sensitivity in wall-bounded flows, it is first necessary to compare estimated velocity fields from wOFV to a known ground truth velocity. Synthetic data represents an idealised testing environment but provides a useful platform where parameters can be easily and independently controlled to understand the baseline wOFV performance and λ parameter sensitivity.

3.1. DNS dataset

The synthetic data test case is derived from direct numerical simulation (DNS) of a turbulent channel flow (Graham et al., 2016) hosted online at John Hopkins Turbulence Database (JHTDB) (Li et al., 2008). Simulation parameters of the DNS in JHTDB are stored in a nondimensional form based on the half-channel height h. The Reynolds numbers based on bulk velocity (U_b), centreline velocity (U_c) and friction velocity (u_τ) are $Re_b = 3.9998 \times 10^4$, $Re_c = 2.2625 \times 10^4$ and $Re_\tau = 999$ respectively. 100 temporally correlated 3D velocity fields are extracted at a grid resolution of $1024 \times 1024 \times 3$ from a subset of the DNS domain that includes the no-slip velocity grid point of the lower wall.

3.2. Particle image generation

Once the velocity fields from the DNS are acquired, it is necessary to determine tracer particle displacements between frames of each image pair as they are advected by the DNS velocity. For the

initial frame of each image pair, synthetic particle tracer locations are initialised from a random distribution for each of the extracted DNS velocity fields. The displacement of each particle in each second frame is computed numerically using an explicit Runge-Kutta scheme (Dormand & Prince, 1980). The velocity fields and particle displacements are then scaled from the nondimensional DNS units to pixel displacements in the image plane such that the maximum image plane velocity magnitude corresponds to ≈ 3.5 px/dt, and the maximum out-of-plane displacement is ≈ 0.8 px/dt. The particle image pixel intensities are determined using classical methods of synthetic particle image generation described in (Raffel et al., 2018). The final particle seeding density is ≈ 0.03 particles per pixel (PPP), which is similar to the experimental data to be presented in section 5. After the images are rendered, the images and ground truth velocity fields are vertically shifted upwards by 160 pixels to create a masked wall region of zero intensity.

4. wOFV assessment using synthetic data

In this section, wOFV performance is assessed using the ground truth DNS data for comparison. In particular, the sensitivity of the wOFV results to the regularization weighting (λ) is evaluated to understand how varying λ affects estimation of the turbulent boundary layer dynamics. wOFV findings are reported for 6 values of $\lambda = [2, 40, 100, 180, 520, 1000]$. This range of λ covers velocity estimates ranging from under-regularized (i.e. visibly noise-dominated) to over-regularized (over-smoothed). The wOFV error throughout the λ range is characterised to identify suitable λ values where the wOFV error outperforms PIV. Section 4.1 analyses velocity estimates as a function of λ considering the entire image domain. Section 4.2 focuses on evaluating λ's effect specifically on the near-wall region velocity and normalisation to boundary layer inner variables.

PIV is also applied to the synthetic data, providing a benchmark to compare wOFV with the current state-of-the-art. A commercial cross-correlation-based PIV software (DaVis 10.0.05, LaVision) was used for PIV processing. The cross-correlation algorithm used 2 and 3 passes for the initial and final Gaussian-weighted IWs of size 64×64 down to 16×16 with 75% overlap. The anisotropic denoising filter in DaVis was applied to the PIV vector fields with the filter strength selected to best minimise the PIV error relative to the DNS data. For both PIV and wOFV the particle images were preprocessed using a min-max filter (Adrian & Westerweel, 2011) to account for changes in particle intensity resulting from out-of-plane motion within the synthetic laser sheet.

4.1. λ sensitivity based on entire image domain

4.1.1. Single image analysis

The influence of λ is first described by evaluating features of the wOFV velocity field within the entire image domain. Vector accuracy over the image is assessed by the normalised root mean square error metric:

$$\varepsilon_u = \sqrt{\frac{1}{n_p} \sum \frac{(U_1 - U_{1,DNS})^2 + (U_2 - U_{2,DNS})^2}{U_{1,DNS}^2 + U_{2,DNS}^2}} \tag{9}$$

In equation 9, n_v is the total number of velocity vectors per image and U_i is the velocity component in the streamwise and wall-normal directions denoted by the subscripts $i = 1, 2$ respectively.

Figure 1 shows the instantaneous velocity field magnitude from a subset of 4 selected λ values of $2, 40, 180, 1000$. These values respectively correspond to under-regularized, under-regularized but equal to PIV error, optimal and over-regularized. For comparison, the true velocity field from the DNS and corresponding velocity field from PIV are also shown. The associated ε_u value for each result is reported above each sub-figure. At $\lambda = 2$, the velocity estimate is under-regularized, leading to fine-scale noise visible as a speckle-like pattern within the velocity field. As λ increases to 40, the noise becomes noticeably suppressed. At $\lambda = 180$, the noise is effectively removed from the velocity field and achieves the lowest ε_u, thus providing the closest agreement with the DNS. This λ value producing the minimum ε_u will be referred to as λ^*. Far beyond λ^* at $\lambda = 1000$, the flow field is considered over-regularized; the noise has been eliminated entirely at the expense of over-smoothing the flow and therefore deviating from the DNS with ε_u nearly doubling. PIV produces a high-quality velocity estimate with ε_u as low as the $\lambda = 40$ wOFV result. With λ^*, a modest improvement in ε_u is achieved, suggesting that wOFV can outperform PIV for the synthetic velocity data.
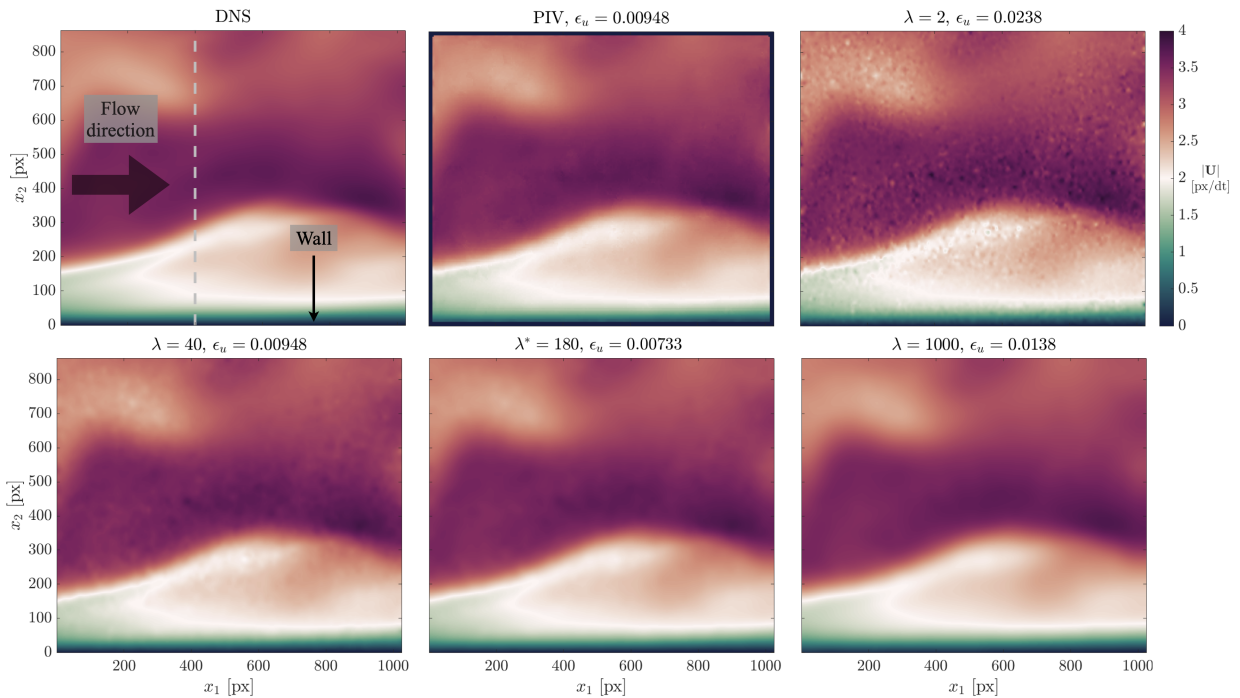

Figure 1. Velocity magnitude for PIV and wOFV (λ=[2,40,180,1000]). The grey dashed line marks the location of the velocity profile analysed in section 4.2.1 - 4.2.2

4.1.2. Image sequence analysis

The findings in Sect. 4.1.1 consider a single image pair from the synthetic dataset. The influence of λ for the complete 100 image sequence, which involves a temporally varying wall-bounded flow,

will be now considered. Figure 2 shows the ε_u values for wOFV at an expanded range of λ values, as well as for PIV across the image sequence. The expanded range includes 2 additional values of $\lambda = 100$ (near optimum) and $\lambda = 520$, (over-regularized but equal to PIV error). The ensemble average $\langle \varepsilon_u \rangle$ values are shown by the bar chart in Figure 5b.

Overall, the error analysis reveals that wOFV can surpass PIV accuracy for a relatively broad range of λ values with a maximum accuracy improvement of 24% compared to PIV on this dataset. The gradual increase in $\langle \varepsilon_u \rangle$ for over-regularized λ values compared to the sharp rise in $\langle \varepsilon_u \rangle$ for under-regularized λ values suggest that in the absence of a ground truth reference, it may be preferable to select for over-regularized as opposed to under-regularized velocity estimates. However, it should be emphasised that $\langle \varepsilon_u \rangle$ represents a spatially averaged value across the entire image domain. It is unlikely that a single λ value is optimal for all locations of the velocity field. This aspect will be further examined in section 4.2.
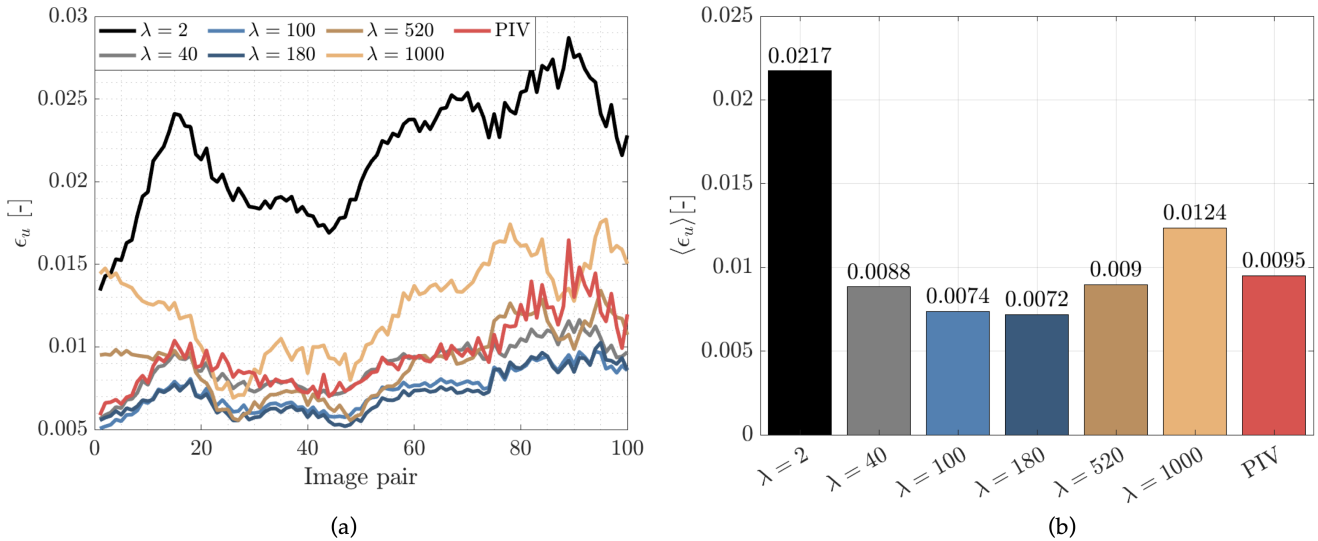

(a)

(b)

Figure 2. Instantaneous ε_u per image pair (a) and mean $< \varepsilon_u >$ for wOFV and PIV across full image sequence (b).

4.2. λ sensitivity in the near-wall region

4.2.1. Viscous sublayer velocity

The viscous sublayer ($y^+ < 5$) region of the mean streamwise velocity profiles $\langle U_1 \rangle$ is presented in Figure 3a, while the wOFV vectors closest to the wall are shown in Figure 3b.

The effect of increasing λ on wOFV is evident in Figure 3b. As λ increases, the streamwise velocity approaching the wall is elevated and increasingly deviates from the no-slip condition at the wall at $x_2 = 0$ as the vector field near the wall becomes oversmoothed. This effect is particularly pronounced for the over-regularized $\lambda = 520$ and $\lambda = 1000$ results, while lower λ results are concentrated around a similar range of $\langle U_1 \rangle = 0.003 - 0.01$ at the wall. Interestingly, it is visible that even at $\lambda^* = 180$, being optimal for the entire image domain, begins displaying a deviation from the DNS as the wall is approached. The tendency for the regularization term to dominate

and oversmooth at motion discontinuities is well-known in image processing literature and is a result of evaluating J_R in a quadratic penalty (Zach et al., 2007). Compared to the DNS and wOFV results, PIV estimates a slightly lower velocity within the resolved PIV region down to $x_2 = 14$. Although relatively minor, this systematic error occurring in the vicinity of the wall is also absent in all of the wOFV results.
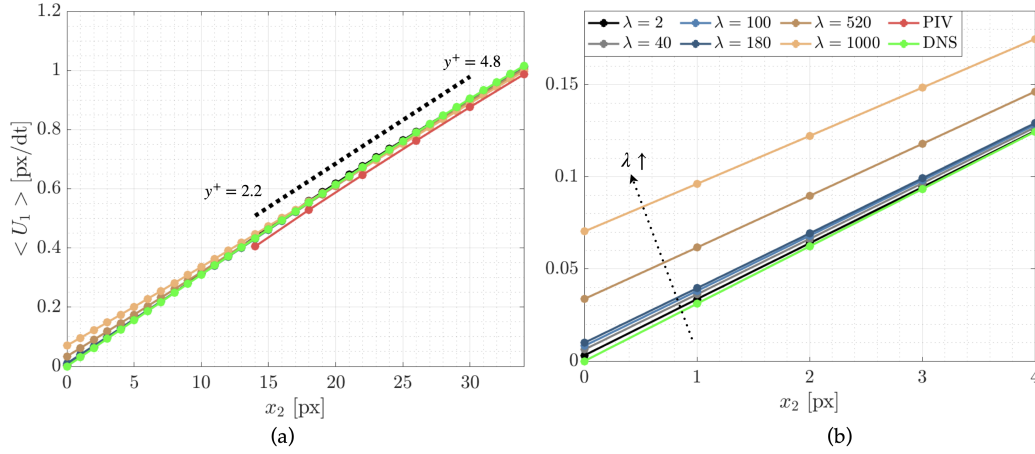

Figure 3. Mean streamwise velocity profiles near the wall taken at the grey dashed line in figure 2. The region used for the γ calculation for PIV is marked by the dashed line.

4.2.2. Near-wall gradient

The calculation of the near-wall gradient γ is performed by using a linear regression for wOFV and PIV. For PIV, linear regression is performed from $y^+ = 4.8$ down to the final vector at $y^+ = 2.2$ as illustrated by the dashed line in Figure 3. For wOFV, the linear regression uses the same $y^+ = 4.8$ starting point, but extends all the way down to the wall excluding 2 pixels above the no-slip pixel at $x_2 = 0$. The regression calculation includes 5 vectors for PIV and 28 vectors for wOFV. A percentage error in γ is calculated by:

$$\varepsilon_\gamma = \frac{|\gamma - \gamma_{DNS}|}{\gamma_{DNS}} \times 100 \tag{10}$$

The mean average of the normalised near-wall gradient error ε_γ across the downstream distance is shown in Figure 4.

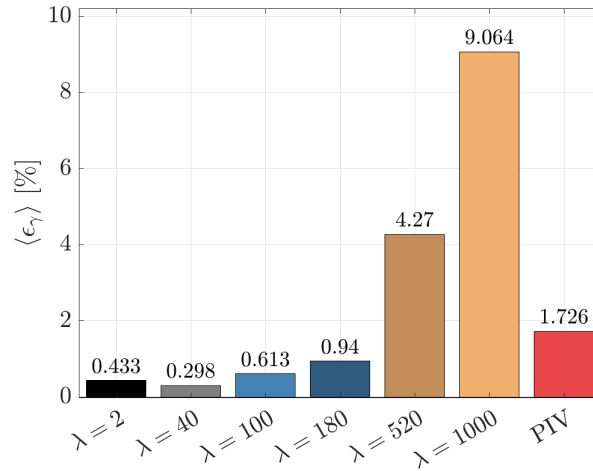**Figure 4.** Mean ε_γ error across the full image downstream distance.

From Figure 4, it can be seen that wOFV results ranging from $\lambda = 2$ to $\lambda^* = 180$ outperform PIV, with impressive errors <1%. The influence of noise in the under-regularized $\lambda = 2$ results in a minor deviation from the minimum ε_γ at $\lambda = 40$. In contrast, the over-regularized $\lambda = 520$ and $\lambda = 1000$ have serious and unacceptable levels of error as a result of the over-smoothing effect described previously in section 4.2.1. The minimum ε_γ achieved at $\lambda = 40$ is a significant improvement of 83% compared to PIV. This minimum occurs at a distinctly lower value than the $\lambda^* = 180$, which, while being optimal for the entire image domain, brings a reduced but still considerable improvement of 45%. Clearly, a slight compromise exists between optimising results for the best average vector accuracy in the entire image domain or for the best estimation of γ at the wall which is necessary for inner scaling of the boundary layer quantities by u_τ. However, it is a positive outcome that the existing regularization method used in wOFV still shows improvements over PIV across a wide range of λ, with $\lambda = 40$ to $\lambda^* = 180$ outperforming PIV on both average vector accuracy ε_u and more notably on ε_γ.

4.2.3. Normalised mean velocity profile

The mean inner-scaled velocity profiles are now analysed to consider the combined effect of λ across the mean streamwise velocity, together with the resulting normalisation by u_τ. The inner scaled profiles are presented in Figure 5, taken at the location marked in Figure 1. Each profile is normalised using its respective u_τ calculated from γ.

When λ increases to the over-regularized $\lambda = 520, 1000$, the near-wall gradient γ becomes over-smoothed and therefore u_τ becomes underestimated. As a result, the calculated y^+ values are slightly decreased while conversely u^+ values are increased as can be understood from examination of equations 3 and 4. This creates a slight vertical, and left offset in the entirety of the profile, particularly evident in $\lambda = 520, 1000$ in Figure 5a. This offset due to normalisation by an underestimated u_τ also has detrimental effects in the very near-wall region as visible in Figure 5b, with severe deviation from the established linear theoretical relation in the viscous sublayer for

$\lambda = 520, 1000$. For the remaining wOFV results that are not over-regularized, there is excellent agreement with the DNS and viscous sublayer. Slight noise in the $\lambda = 2$ result is present in the logarithmic region however. PIV is broadly in agreement with the DNS, but shows a slight discrepancy in the logarithmic region but not to the extent of $\lambda = 520, 1000$. PIV resolves down to a minimum $y^+ = 2.21$ in the viscous sublayer. Excluding the over-regularized $\lambda = 520, 1000$, wOFV resolves 2 decades in wall units further than PIV down to $y^+ = 0.15$ while maintaining excellent agreement with the DNS. While λ^* was previously shown to be slightly sub-optimal in minimising ε_γ compared to $\lambda = 40$ as discussed in section 4.2.2, the final outcome on the inner-scaled profiles is effectively indistinguishable. Assuming a suitable λ is selected, these results show highly encouraging performance characteristics of wOFV since the increased accuracy produces improvements in both accurately resolving the instantaneous velocity across the extent of the boundary layer and normalisation of mean flow properties compared to PIV.
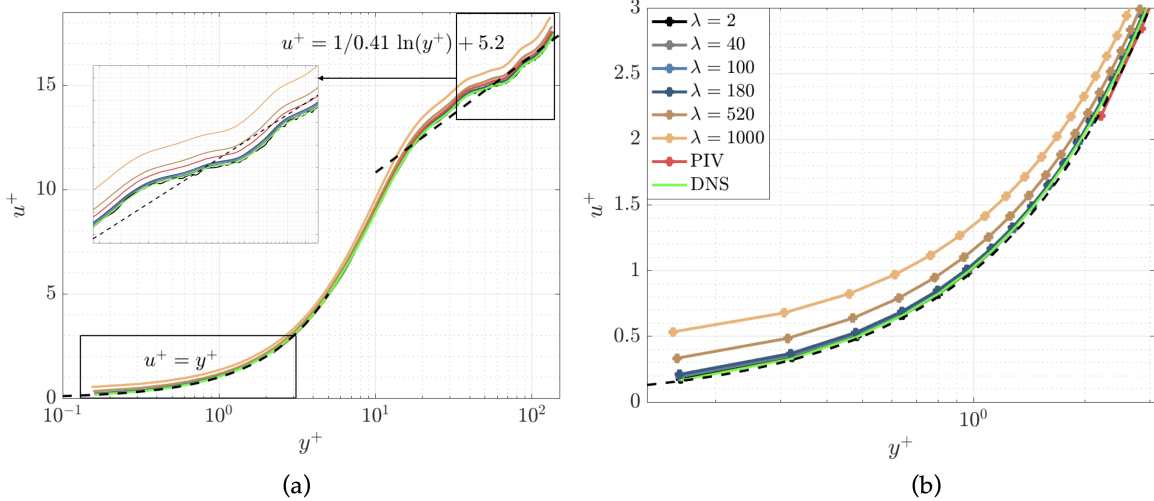

Figure 5. Inner scaled mean velocity profiles. Theoretical relations for the viscous sublayer and logarithmic region are shown in the dashed lines.

5. Experimental test case

It is important to evaluate the performance of the method on a real experimental dataset which departs from the simplified modelling assumptions inherent in synthetic data. Naturally, the absence of a ground truth velocity field for comparison means determining the truly optimal λ is not possible. wOFV results from 3 values of $\lambda = 0.1, 2, 20$ will be presented. Compared to the synthetic data, the reduced λ range is due to a significantly steeper velocity gradient at the wall, together with the viscous sublayer occupying a smaller image plane pixel distance. The current experimental dataset is therefore significantly stricter regarding selection of an appropriate λ, which will be justified a posteriori based on physical principles. These results will also be compared to those obtained from correlation-based PIV processing.

5.1. Experimental setup

The near-wall velocity test case was measured in an experimental facility that has been established for atmospheric side-wall quenching (SWQ) investigations, see (Jainski et al., 2018) (Kosaka et al., 2018) (Kosaka et al., 2020) (Zentgraf et al., 2021) (Zentgraf et al., 2022) for details. For demonstrating the capabilities of wOFV in a turbulent boundary layer, this study used the SWQ-burner as a flow facility under non-reacting conditions in ambient temperature. The flow at the outlet of the burner impinges onto the leading edge of stainless steel wall, forming a developing turbulent boundary layer along the wall. The Reynolds number based on the hydraulic diameter of the nozzle exit at the outlet of the burner was $Re = 5900$ and the turbulence intensity of the flow was 6-7%. The flow was seeded with Al_2O_3 particles illuminated using a dual-cavity Nd:YAG PIV laser (New Wave Research, Gemini PIV, G200, 10 Hz, 532 nm). A low-speed (10 Hz) two-dimensional, two-component particle image velocimetry (2D2C-PIV) was applied. Both PIV pulses were separated by $\delta t = 40\mu$s. The imaged field of view (FOV) featured dimensions of $(\triangle x_1, \triangle x_2) \approx (40mm, 47.5mm) = 2184\text{px} \times 2580\text{px}$. For velocimetry processing, the images are cropped to $(\triangle x_1, \triangle x_2) \approx (38mm, 38mm) = 2048\text{px} \times 2048\text{px}$. This reduced FOV begins at the leading edge where the origin of the streamwise (x_1) and wall-normal (x_2) coordinates are defined.

Images were pre-processed with subtraction of the ensemble minimum image followed by a min-max intensity normalization (Adrian & Westerweel, 2011). PIV vector processing was performed using multi-pass correlation with an initial IW size of 64×64 down to 16×16 with 75% overlap. The resulting 1 vector per 4×4 pixels corresponds to a vector spacing of $74.3\mu m^2$ and PIV resolution of approximately $297.2\mu m^2$. The per-pixel vector spacing of wOFV result is equivalent to 1 vector per $18.6\mu m^2$.

5.1.1. Mean velocity Profile

The near-wall velocity profiles are shown in Figure 6a, with the inner-scaled forms in Figure 6b. The near-wall gradient γ is calculated from the ensemble average streamwise velocity fields using a linear regression in a similar manner to that described in the section 4.2. $\langle U_1 \rangle$ profiles are taken $36.3mm$ downstream from the leading edge and averaged over across a $2mm$ streamwise x_1 distance for both techniques. In the viscous sublayer ($y^+ < 5$), there are 15 velocity vectors for wOFV compared to 3 velocity vectors for PIV. The linear regression for wOFV uses 12 of these vectors avoiding the 2 vectors nearest to the wall. The calculation for PIV uses only 2 out of the 3 available vectors since the final PIV vector nearest to the wall is frequently spurious. As seen in equation 2, the estimation of γ has a direct effect on normalisation to wall units through u_τ. Incorrect estimates of γ therefore result in a strong offset from the theoretical $u^+ = y^+$ shown by the dotted green line in Figure 6b. Comparison with this linear relation will be used as an approximate measure to judge the quality of the near-wall vectors in the absence of a ground truth velocity.

In Figure 6a, the profiles away from the wall above 1mm can be seen to be in excellent agreement. For $x_2 < 1mm$, the wOFV $\lambda = 20$ profile shows increasing deviation from other profiles as the wall is approached because this result is over-regularized. The excessive smoothing strongly washes out the velocity gradient at the wall, creating an underestimate of u_τ. The resulting nor-

malisation creates a strong deviation from $u^+ = y^+$ visible in Figure 6b for the $\lambda = 20$ result and confirms that this λ value is not appropriate for normalising boundary layer quantities since γ estimation is greatly compromised. Good agreement is shown between $\lambda = 0.1, 2$ and PIV until $x_2 < 0.4mm$, where PIV shows a milder gradient for $0.3 < x_2 < 0.4mm$ followed by a sharper velocity gradient at the last PIV data point. As will be shown, the last PIV data point is susceptible to noise at the wall, which can bias the interpreted flow behaviour. Considering Figure 6b, the $\lambda = 2$ result aligns closely with the $u^+ = y^+$ relation, remaining in good agreement with a discrepancy of $0.17\delta u^+$ at the final vector. $\lambda = 2$ can therefore be considered an approximate but phyiscally justified selection for this experimental dataset as it results in a successful collapse of the mean profiles onto the well-established linear viscous sublayer relation. The PIV results is similarly aligned with $\lambda = 2$ in regions away from the viscous sublayer. Within the linear region, the elevated velocities compared to wOFV, as seen in Figure 6a, manifest in a deviation from $u^+ = y^+$ with the final PIV vector diverging from the linear trend of the others. The $\lambda = 0.1$ wOFV profile is offset slightly below $u^+ = y^+$ due to noise from under-regularization, which leads to an error in the estimation of γ. High frequency noise in the $\lambda = 0.1$ profile is also visible in the u^+ estimates for $y^+ > 75$.
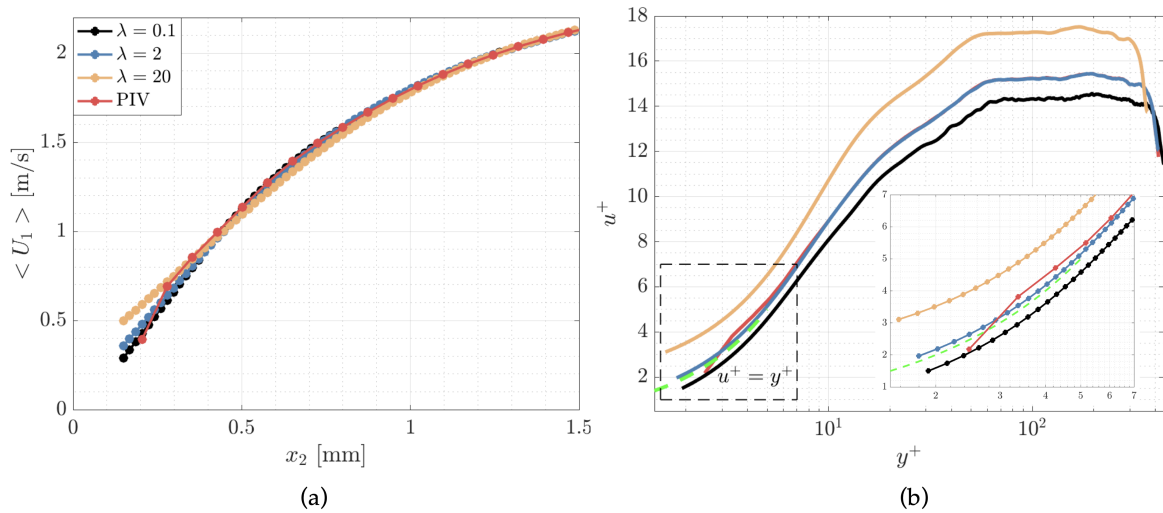

Figure 6. Mean streamwise velocity profiles a) and inner-scaled forms b).

5.1.2. Normalised velocity fluctuations

Figure 7 shows profiles of the normalised streamwise velocity fluctuations $\langle u_1 u_1 \rangle^+$, where $u_1 = U_1 - \langle U_1 \rangle$. Similarly to the mean values, the fluctuation profiles are averaged across the $2mm$ streamwise distance with the extent of a single standard deviation of these fluctuations illustrated by the shaded area. Since the turbulent velocity fluctuations do not have a common description in the near-wall region like the mean streamwise velocity, the extent of the standard deviation of these values within this $2mm$ averaging distance can be considered indicative of the reliability of the velocity estimate and its susceptibility to error.

In Figure 7, each curve follows a relatively similar trend from $y^+ = 200$ to $y^+ = 10$; $\langle u_1, u_1 \rangle^+$ values increase from the free stream region and exhibit a local maximum within the buffer layer

at $y^+ \approx 10$. From $y^+ = 10$ towards the wall, each curve exhibits different trends. For PIV, $\langle u_1, u_1 \rangle^+$ values continue to rise, before a slight decrease and followed by a substantial increase within the last 2 vectors. This trend is non-physical as the turbulent fluctuations should become suppressed in very close proximity to the wall. The large variation shown by the shaded region demonstrates that PIV is particularly susceptible to errors near the wall which are also in part caused by the reflection pattern and reduced SNR. Compared to the other wOFV results, $\lambda = 0.1$ in general shows a wider variation in $\langle u_1, u_1 \rangle^+$, particularly for $y^+ < 40$, due to noise form under-regularization artificailly increasing the fluctuation intensity. However, below $y^+ = 10$, this variation is still less than for PIV. The elevated fluctuation intensities for $\lambda = 20$ in the buffer and viscous sublayer regions are caused by the under-estimation of γ which creates a noticeable vertical and left offset when normalising to wall units, similarly to the $\lambda = 20$ mean profile shown in Figure 6b. All wOFV profiles initially show an expected decrease below the peak fluctuation intensity at $y^+ = 10$. $\lambda = 0.1$ and $\lambda = 20$ eventually show an increase in $\langle u_1, u_1 \rangle^+$ and plateau for $y^+ < 3$ however. $\lambda = 2$ continues the expected $\langle u_1, u_1 \rangle^+$ decrease into the viscous sublayer, furthering support for the suitability of selecting $\lambda = 2$ as the regularization weighting based on physical principles.

Overall, the findings demonstrate the impressive vector resolution from wOFV in boundary layer velocity measurements, and reveal the potential to measure turbulent velocity fluctuations more accurately and reliably in the vicinity of the wall where PIV encounters difficulty.
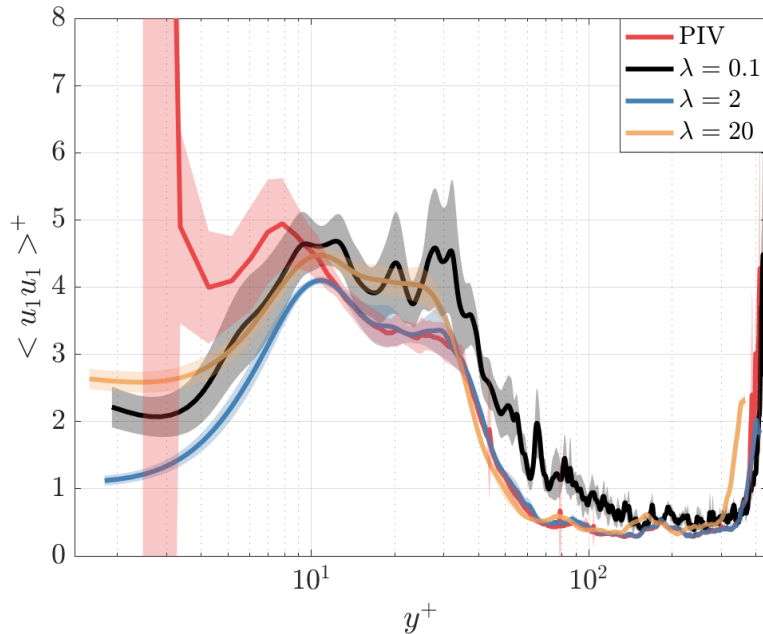

Figure 7. Streamwise turbulent fluctuations.

6. Conclusions

The performance of a wavelet-based optical flow velocimetry (wOFV) method was assessed on synthetic and experimental particle images of turbulent wall-bounded flows. The ability to extract

high-resolution estimates of instantaneous, mean and derived flow properties was evaluated in the vicinity of the wall. The sensitivity to the regularization parameter λ of these results was also analysed; an aspect largely not discussed in other OFV works.

Results on synthetic particle images indicate improved accuracy over PIV. wOFV was able to outperform optimised PIV results in overall vector accuracy across a broad range of variation of the regularization parameter λ. Analysis of the near-wall gradient γ revealed more improvements in accuracy over PIV. It was found that the optimal λ for overall vector accuracy (λ^*) was a higher value than that which produces the best estimates of the near-wall gradient γ and therefore wall shear stress u_τ. Despite this slight compromise in optimal regularization, λ^* was still able to outperform PIV on γ estimates which lead to more accurate normalisation of mean boundary layer quantities and overall vector accuracy.

wOFV was applied to an experimental dataset of a turbulent boundary layer and compared to results from PIV. Based on the theoretical relations of the linear viscous sublayer, an approximate but theoretically justified λ was determined. Compared to PIV, this λ result was able to more accurately resolve the mean velocity nearer to the wall in the viscous sublayer. While PIV still performed acceptably in resolving the mean velocity near the wall, estimates of the turbulent velocity fluctuations featured significantly increased error evidenced through a non-physical increase in turbulent intensity in the viscous sublayer and extremely large variation in local streamwise turbulence intensity. In comparison, wOFV does not exhibit these artefacts which positively indicates that wOFV is less susceptible to the common challenges affecting PIV near boundaries.

Overall, this study demonstrates progress in diagnostic capability and accuracy by application of wOFV to wall-bounded flows together with relevant considerations for justifying parameter selection using physical principles. The authors point out that the wOFV algorithm does not feature direct modifications or explicit constraints for handling physical boundaries or image discontinuities. It is expected that such enhancements, although beyond the scope of current work, would bring further improvement such as decreased sensitivity to the over-smoothing effect from high λ and better the techniques' potential for resolving flow in more complex geometries.

Acknowledgements

References

Adrian, R. J., & Westerweel, J. (2011). *Particle image velocimetry* (No. 30). Cambridge university press.

Aubert, G., Deriche, R., & Kornprobst, P. (1999). Computing optical flow via variational techniques. *SIAM Journal on Applied Mathematics*, *60*(1). doi: 10.1137/S0036139998340170

Black, M. J., & Anandan, P. (1996). The robust estimation of multiple motions: Parametric and piecewise-smooth flow fields. *Computer Vision and Image Understanding*, *63*(1). doi: 10.1006/cviu.1996.0006

Cai, S., Mémin, E., Dérian, P., & Xu, C. (2018). Motion estimation under location uncertainty for turbulent fluid flows. *Experiments in Fluids*, *59*(1). doi: 10.1007/s00348-017-2458-z

Corpetti, T., Heitz, D., Arroyo, G., Mémin, E., & Santa-Cruz, A. (2006). Fluid experimental flow estimation based on an optical-flow scheme. *Experiments in Fluids*, *40*(1). doi: 10.1007/s00348-005-0048-y

Corpetti, T., Mémin, Ã., & Pérez, P. (2002). Dense estimation of fluid flows. *IEEE Transactions on Pattern Analysis and Machine Intelligence*, *24*(3). doi: 10.1109/34.990137

Dérian, P., Héas, P., Herzet, C., & Mémin, E. (2013). Wavelets and optical flow motion estimation. *Numerical Mathematics*, *6*(1). doi: 10.4208/nmtma.2013.mssvm07

Ding, C. P., Peterson, B., Schmidt, M., Dreizler, A., & Böhm, B. (2019). Flame/flow dynamics at the piston surface of an IC engine measured by high-speed PLIF and PTV. *Proceedings of the Combustion Institute*, *37*(4), 4973–4981. doi: 10.1016/J.PROCI.2018.06.215

Dormand, J. R., & Prince, P. J. (1980, 3). A family of embedded Runge-Kutta formulae. *Journal of Computational and Applied Mathematics*, *6*(1), 19–26. doi: 10.1016/0771-050X(80)90013-3

Graham, J., Kanov, K., Yang, X. I., Lee, M., Malaya, N., Lalescu, C. C., … Meneveau, C. (2016). A web services accessible database of turbulent channel flow and its use for testing a new integral wall model for LES. *Journal of Turbulence*, *17*(2). doi: 10.1080/14685248.2015.1088656

Heás, P., Herzet, C., Meáÿ£in, E., Heitz, D., & Mininni, P. D. (2013). Bayesian estimation of turbulent motion. *IEEE Transactions on Pattern Analysis and Machine Intelligence*, *35*(6). doi: 10.1109/TPAMI.2012.232

Héas, P., Mémin, E., Heitz, D., & Mininni, P. D. (2012). Power laws and inverse motion modelling: Application to turbulence measurements from satellite images. *Tellus, Series A: Dynamic Meteorology and Oceanography*, *64*(1). doi: 10.3402/tellusa.v64i0.10962

Horn, B. K., & Schunck, B. G. (1981). Determining optical flow. *Artificial Intelligence*, *17*(1-3). doi: 10.1016/0004-3702(81)90024-2

Jainski, C., Rißmann, M., Jakirlic, S., Böhm, B., & Dreizler, A. (2018). Quenching of Premixed Flames at Cold Walls: Effects on the Local Flow Field. *Flow, Turbulence and Combustion*, *100*(1). doi: 10.1007/s10494-017-9836-8

Kadri-Harouna, S., Dérian, P., Héas, P., & Mémin, E. (2013). Divergence-free wavelets and high order regularization. *International Journal of Computer Vision*, *103*(1). doi: 10.1007/s11263-012 -0595-7

Kähler, C. J., Astarita, T., Vlachos, P. P., Sakakibara, J., Hain, R., Discetti, S., … Cierpka, C. (2016). Main results of the 4th International PIV Challenge. *Experiments in Fluids*, *57*(6). doi: 10.1007/ s00348-016-2173-1

Kähler, C. J., Scharnowski, S., & Cierpka, C. (2012a). On the resolution limit of digital particle image velocimetry. *Experiments in Fluids*, *52*(6). doi: 10.1007/s00348-012-1280-x

Kähler, C. J., Scharnowski, S., & Cierpka, C. (2012b). On the uncertainty of digital PIV and PTV near walls. *Experiments in Fluids*, *52*(6). doi: 10.1007/s00348-012-1307-3

Kapulla, R., Hoang, P., Szijarto, R., & Fokken, J. (2011). Parameter sensitivity of optical flow applied to PIV Images. *Proceedings of the Fachtagung âĂIJLasermethoden in der StrömungsmesstechnikâĂİ, Ilmenau, Germany*, 6–8.

Kosaka, H., Zentgraf, F., Scholtissek, A., Bischoff, L., Häber, T., Suntz, R., … Dreizler, A. (2018). Wall heat fluxes and CO formation/oxidation during laminar and turbulent side-wall quenching of methane and DME flames. *International Journal of Heat and Fluid Flow*, *70*. doi: 10.1016/ j.ijheatfluidflow.2018.01.009

Kosaka, H., Zentgraf, F., Scholtissek, A., Hasse, C., & Dreizler, A. (2020). Effect of Flame-Wall Interaction on Local Heat Release of Methane and DME Combustion in a Side-Wall Quenching Geometry. *Flow, Turbulence and Combustion*, *104*(4). doi: 10.1007/s10494-019-00090-4

Li, Y., Perlman, E., Wan, M., Yang, Y., Meneveau, C., Burns, R., … Eyink, G. (2008). A public turbulence database cluster and applications to study Lagrangian evolution of velocity increments in turbulence. *Journal of Turbulence*, *9*. doi: 10.1080/14685240802376389

Mallat, S. (2009). *A Wavelet Tour of Signal Processing*. doi: 10.1016/B978-0-12-374370-1.X0001-8

Prandtl, L. (1904). Über Flüssigkeitsbewegung bei sehr kleiner Reibung ("Motion of Fluids with Very Little Viscosity"). *Internationalen Mathematiker-Kongresses*.

Raffel, M., Willert, C. E., Scarano, F., Kähler, C. J., Wereley, S. T., & Kompenhans, J. (2018). *Particle Image Velocimetry: A Practical Guide*.

Renaud, A., Ding, C. P., Jakirlic, S., Dreizler, A., & Böhm, B. (2018, 6). Experimental characterization of the velocity boundary layer in a motored IC engine. *International Journal of Heat and Fluid Flow*, *71*, 366–377. doi: 10.1016/J.IJHEATFLUIDFLOW.2018.04.014

Ruhnau, P., & Schnörr, C. (2006). Optical Stokes flow estimation: an imaging-based control approach. *Experiments in Fluids*, *42*(1). doi: 10.1007/s00348-006-0220-z

Ruhnau, P., Stahl, A., & Schnörr, C. (2007). Variational estimation of experimental fluid flows with physics-based spatio-temporal regularization. *Measurement Science and Technology*, *18*(3). doi: 10.1088/0957-0233/18/3/027

Schmidt, B. E., & Sutton, J. A. (2019). High-resolution velocimetry from tracer particle fields using a wavelet-based optical flow method. *Experiments in Fluids*, *60*(3). doi: 10.1007/s00348-019-2685-6

Schmidt, B. E., & Sutton, J. A. (2020). Improvements in the accuracy of wavelet-based optical flow velocimetry (wOFV) using an efficient and physically based implementation of velocity regularization. *Experiments in Fluids*, *61*(2). doi: 10.1007/s00348-019-2869-0

Schröder, A., Geisler, R., Staack, K., Elsinga, G. E., Scarano, F., Wieneke, B., . . . Westerweel, J. (2011). Eulerian and Lagrangian views of a turbulent boundary layer flow using time-resolved tomographic PIV. In *Experiments in fluids* (Vol. 50). doi: 10.1007/s00348-010-1014-x

Stanislas, M., Okamoto, K., Kähler, C. J., & Westerweel, J. (2005). Main results of the Second International PIV Challenge. In *Experiments in fluids* (Vol. 39). doi: 10.1007/s00348-005-0951-2

Stark, M. (2013). *Optical Flow PIV: Improving the Accuracy and Applicability of Particle Image Velocimetry*. ETH, Department of Mechanical and Process Engineering. Retrieved from `https://books.google.co.uk/books?id=p92MnQEACAAJ`

Willert, C. E. (2015). High-speed particle image velocimetry for the efficient measurement of turbulence statistics. *Exp Fluids*, *56*, 17. doi: 10.1007/s00348-014-1892-4

Yuan, J., Schnörr, C., & Mémin, E. (2007). Discrete orthogonal decomposition and variational fluid flow estimation. *Journal of Mathematical Imaging and Vision*, *28*(1). doi: 10.1007/s10851-007-0014-9

Zach, C., Pock, T., & Bischof, H. (2007). A Duality Based Approach for Realtime TV-{\itshape L}<Superscript>1</Superscript> Optical Flow. In *Pattern recognition* (Vol. 4713).

Zentgraf, F., Johe, P., Cutler, A. D., Barlow, R. S., Böhm, B., & Dreizler, A. (2021). Classification of flame prehistory and quenching topology in a side-wall quenching burner at low-intensity turbulence by correlating transport effects with CO2, CO and temperature. *Combustion and Flame*. doi: 10.1016/j.combustflame.2021.111681

Zentgraf, F., Johe, P., Steinhausen, M., Hasse, C., Greifenstein, M., Cutler, A. D., . . . Dreizler, A. (2022). Detailed assessment of the thermochemistry in a side-wall quenching burner by simultaneous quantitative measurement of CO2, CO and temperature using laser diagnostics. *Combustion and Flame*, *235*. doi: 10.1016/j.combustflame.2021.111707